Chemical Science

ROYAL SOCIETY OF CHEMISTRY

EDGE ARTICLE

View Article Online
View Journal

Cite this: DOI: 10.1039/d6sc02206e

All publication charges for this article have been paid for by the Royal Society of Chemistry

Deconstructing the black box of zeolite crystallization gels by species-specific isolation

Kexin Yan,†[a] Feng Lin,†[a] Zhaoqi Ye,[a] Yifan Zhang,[a] Yang Zhao,[a] Zhangping Shi,[c] Di Pan,[a] Yahong Zhang,[a] Hongbin Zhang *[b] and Yi Tang *[a]

The crystallization of zeolites in gel-based systems, the cornerstone of their industrial synthesis, has long remained a "black box" due to the inability to characterize specific aluminosilicate species within the amorphous network. This obscurity precludes rational design. Herein, we report a deconstruction-dialysis methodology that disassembles the gel and isolates the entire suite of particulate intermediates. Applying this to the MTW-type zeolite, we quantitatively identify a hierarchy of species: long-range-ordered crystals (MTW-*t*-C), short-range but highly ordered precursors (MTW-*t*-HOP), poorly ordered particles (POPs), and monomers/oligomers. We demonstrate that HOPs are the primary building blocks for crystal growth *via* nonclassical particle attachment. More importantly, by tracking the evolution of these species and combining with the Kolmogorov–Johnson–Mehl–Avrami (KJMA) model, we delineate the crystallization into three stages: nucleation, particle attachment, and molecular addition. We reveal that the final properties of the zeolite are governed by a dynamic competition between the rate of HOP attachment and that of structural/elemental maturation (dealumination). This competition dictates the temporal evolution of defects, porosity, and composition. Our work dismantles the gel black box by establishing a species-resolved crystallization pathway, offering a universal strategy for mechanistic understanding in complex media and thereby paving the way for the precise synthesis of zeolites.

Received 17th March 2026
Accepted 15th June 2026

DOI: 10.1039/d6sc02206e

rsc.li/chemical-science

Introduction

Zeolites, microporous crystalline aluminosilicates, are indispensable in modern industrial processes[1,2] such as petroleum refining,[3] environmental remediation,[4–6] and green energy technologies.[7] Their exceptional catalytic activity and molecular-sieving capabilities align with the principles of green chemistry, sustaining a global market valued at $3.42 billion and projected to reach $6 billion by 2030. However, the rational design of cost-effective, high-performance zeolites is impeded by fundamental gaps in understanding their crystallization mechanisms. This is particularly true for gel-based systems, which are the workhorse of industrial production yet remain largely a "black box" at the meso- and microscopic scales in gel-based systems.[8]

To overcome this fundamental barrier, current mechanistic understanding of zeolite crystallization stems first from studies of clear-solution syntheses. The low concentrations, homogeneity, and optical transparency of these systems enable real-time monitoring and the application of advanced *in situ* characterization techniques. Seminal contributions from several groups have observed short-range ordered precursor species,[9–12] elucidated nucleation pathways and precursor dynamics in such systems, revealing intricate interplays between classical and nonclassical crystallization mechanisms.[13–18] Nonetheless, clear-solution routes are applicable to only a limited range of zeolite frameworks and provide minimal insight into the industrially predominant gel-based processes.

In contrast, industrial production scenarios favored gel-based systems because of their cost efficiency and high yields.[8] However, characterized by high aluminosilicate concentrations and complex hydrogen-bonded networks,[19–22] gel-based systems present a formidable analytical challenge. These systems are often heterogeneous, forming solid-like blocks with spatially non-uniform concentration profiles. Consequently, nucleation events, driven by local supersaturation, are inherently stochastic, uncontrollable, and notoriously difficult to observe directly. While techniques such as transmission electron microscopy (TEM)[23–25] and *in situ* atomic force

[a]*Department of Chemistry, College of Smart Materials and Future Energy, State Key Laboratory of Porous Materials for Separation and Conversion, Shanghai Key Laboratory of Molecular Catalysis and Innovative Materials, and Laboratory of Advanced Materials, Fudan University, Shanghai 200433, P. R. China. E-mail: yitang@fudan.edu.cn*

[b]*Key Laboratory of Silicate Cultural Heritage Conservation (Ministry of Education), Institute for the Conservation of Cultural Heritage, School of Cultural Heritage and Information Management, Shanghai University, Shanghai, 200444, China. E-mail: zhang-hongbin@shu.edu.cn*

[c]*State Key Laboratory of Green Chemical Engineering and Industrial Catalysis, SINOPEC Shanghai Research Institute of Petrochemical Technology, Shanghai 201208, China*

† Kexin Yan and Feng Lin contributed equally.

microscopy (AFM)[26] have identified nascent crystalline domains, these nuclei remain embedded within a vast excess of amorphous gel, obscuring their initial form and evolution. The primary obstacle lies in the lack of long-range order in key precursor species, which renders them indistinguishable from the amorphous network using conventional characterization methods. Consequently, critical information regarding the species governing nonclassical and classical growth pathways is effectively lost within the gel.

The industrial reliance on gel-based synthesis underscores the critical need to demystify these systems. Gel matrices host heterogeneous and multiphasic intermediates, such as worm-like precursors (WLPs),[21,27] whose structural evolution has been inferred only indirectly from bulk-phase analysis or non-selective etching.[23,28,29] Fundamental questions thus remain unresolved: how do disordered aluminosilicate species transition into ordered crystalline frameworks? What factors govern precursor assembly and phase selection? Addressing these questions demands breakthroughs in the speciation and analysis of gel-confined intermediates.

Herein, we report a transformative methodology that unlocks the "black box" of zeolite gel-system crystallization by achieving its complete deconstruction. Using MTW-type zeolite as a model system, we introduce a protocol that isolates and characterizes all particulate species present during crystallization. This approach reveals a well-defined hierarchy of aluminosilicate intermediates, comprising (1) long-range-ordered early crystals (C), (2) short-range but highly ordered particle precursors (HOPs), (3) poorly ordered particles (POPs), and (4) monomers/oligomers. We conclusively identify HOPs as the critical building blocks for crystal growth and elucidate their dynamic transformation pathways at the mesoscopic and molecular scales. Our work establishes a novel paradigm for decoding speciation and nonclassical crystallization mechanisms in gels, bridging the long-standing gap between industrial synthesis practices and fundamental materials science.

Results and discussion

"Deconstruction-dialysis" method to unlock the gel black box

We select the MTW-type zeolite synthesized under low H_2O/SiO_2 conditions as a model system to investigate the gel crystallization mechanism, because our previous research indicates that this MTW system might be deconstructed, due to its formation *via* nanoparticle assembly and the presence of intermediate species with distinct size differences.[24] The crystallization kinetic curve (Fig. 1a) was obtained by combining the relative crystallinity variation (Fig. S1). After the induction period, the system forms a solid-like bulk gel within *ca.* 24–40 hours (Fig. 1a-I and Fig. S2a–d), due to extensive cross-linking and agglomeration of aluminosilicate species. Upon further hydrothermal processing, the gel transitions from translucent to milky white and eventually collapses into a free-flowing solution after 40 hours (Fig. 1a-II and S2e), indicative of the progressive conversion of the gel into MTW zeolite. The final product MTW-72 (Fig. 1a-III and S2f) comprises mesocrystals of 1200–1500 nm, which are aggregates of nanocrystalline domains (<50 nm) with highly rough surfaces (Fig. S3f and S4f), suggesting a nonclassical crystallization pathway dominated by particle attachment.[24]

However, direct visualization of the intact gel network (MTW-*t*-Gel) by SEM and TEM fails to clearly resolve the MTW crystals or aluminosilicate precursors embedded within the amorphous network (Fig. S3 and S4), impeding mechanistic analysis. To address this, we sought to develop a method for classifying and extracting the distinct particulate species from the gel. Inspection of MTW-28-Gel by TEM (Fig. S4b and G–I) revealed well-defined MTW crystals with clear lattice fringes at the edges, suggesting that larger, crystalline entities could be distinguished from the surrounding, lower-contrast precursors. Furthermore, by conducting sectioning on the MTW-28-Gel, the same differences between the crystalline domains and the amorphous gel could be observed (Fig. S5). This once again indicates the presence of potential crystal species within the gel. These observations, coupled with the known particle size evolution during crystallization,[24] suggested that centrifugal separation based on particle size could effectively isolate large MTW crystals from the worm-like precursors (WLPs). But this is not enough. The XRD of the early MTW-*t*-Gel samples showed peak formation at 5–10°, which was completely different from that of the amorphous SiO_2 samples, suggesting that there might be some short-range ordered species in the gel.[30] Therefore, a critical challenge remained: identifying dissolution conditions that disrupt the gel network without compromising the structural integrity of short-range ordered intermediates.

We established a rational disassembly protocol involving TEAOH dissolution and centrifugal separation, yielding distinct species based on size and structural order (Fig. 1b). Prior to disassembly, a pre-water washing operation (Step I-1) was performed on freeze-dried MTW-*t*-Gel samples to remove soluble species involved in the molecular addition (MA) process. The gel was then dissolved using a TEAOH solution (the structure-directing agent, SDA) (Step I-2), leveraging its efficacy in disrupting the gel network while preserving short-range order. Subsequent centrifugation (Step II-1 and II-3) of the MTW-28-Gel disassembly solution yielded the MTW-28-C species (Fig. 1c). This species consists of particles ~600 nm in size, exhibits enhanced MTW XRD diffraction intensity (Fig. 1e), and possesses well-developed micropores (Fig. 1f), confirming the successful isolation of well-crystalline MTW crystals.

Dialysis of the centrifuged supernatant (Step II-2) afforded a distinctly different sample, MTW-28-HOP (Fig. 1d). In contrast to MTW-28-C, MTW-28-HOP comprises much smaller particles (~15 nm) and lacks long-range order, as evidenced by the absence of MTW diffraction peaks in XRD (Fig. 1e). However, Ar physisorption reveals the presence of primary micropores (Fig. 1f and S6), indicating the formation of a short-range ordered structure with incipient pore channels.

The successful isolation of MTW-28-C and MTW-28-HOP allowed us to validate the robustness of the "deconstruction-dialysis" method. Control experiments demonstrated that omitting the pre-water washing step did not alter the yield of MTW-28-C and HOPs (Fig. S7a), confirming that the MA process was effectively eliminated by washing and that the washing step

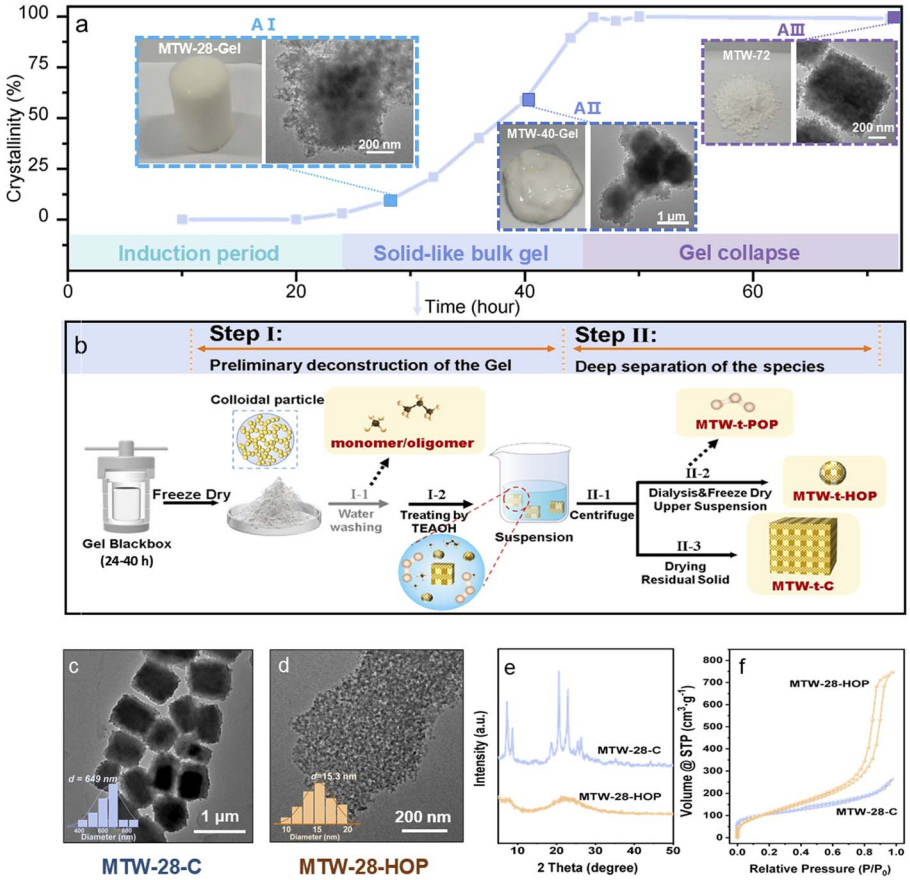

Fig. 1 The crystallization kinetics of MTW zeolite, and the schematic diagram and rationality of the deconstruction-dialysis method. (a) Crystallization kinetics curves of typical MTW synthesis systems, inset: optical images of macroscopic morphology and TEM images of microscopic morphology of the samples. (b) Schematic diagram of the "deconstruction-dialysis" decomposition method. TEM images of (c) MTW-28-C and (d) MTW-28-HOP; inset: particle size distribution. (e) XRD and (f) Ar adsorption and desorption isotherms of MTW-28-C and MTW-28-HOP.

does not impact the insoluble gel-bound species. This finding also implies that the protocol can be simplified if the focus is solely on obtaining the particulate intermediates C and HOPs. Furthermore, varying the TEAOH concentration within a specific range during disassembly had a negligible effect on the yields of MTW-*t*-C and HOPs (Fig. S7b), even when the concentration was increased to nearly twice that of the synthetic system (1.5 M), indicating that the separation is governed by intrinsic physicochemical barriers (*e.g.*, size and structural order) within the gel, rather than being an artifact of the disassembly conditions. However, at a lower concentration (0.1 M), we abnormally collected more species by centrifugation. TEM observation revealed that these species simultaneously included well-crystallized C species and unreconstructed gel parts (Fig. S8), indicating that sufficient alkaline conditions are still required to completely deconstruct the gel.

TEM imaging of the disassembly solution prior to dialysis revealed MTW-28-HOP particles interconnected by colloidal species (Fig. S9), which were removed after dialysis. This observation indicates that the disassembly process breaks down a significant fraction of poorly ordered, insoluble species into monomeric and oligomeric aluminosilicates, which are eliminated during dialysis. To achieve a complete mass balance and fully deconstruct the gel, we quantified this fraction by subtracting the masses of C, HOPs, gel-bound water, and template from the total mass of MTW-28-Gel. This poorly ordered particulate fraction was denoted as MTW-28-POP (poorly ordered particles).

Ultimately, the optimized deconstruction-dialysis method (Fig. 1b) enables the comprehensive fractionation of the gel into four distinct categories based on size and structural order (Table 1): MTW-*t*-C (long-range and highest ordered crystals), MTW-*t*-HOP (short-range but highly ordered precursors), MTW-*t*-POP (poorly ordered particles), and soluble monomers/oligomers. This complete speciation provides the foundation for a detailed analysis of the crystallization pathway, as discussed in the crystallization analysis section.

Novel zeolite intermediates MTW-*t*-C and HOPs

Applying the deconstruction-dialysis method to MTW-*t*-Gel samples at various crystallization times yielded a series of MTW-*t*-C (Fig. 2) and HOP (Fig. 3) samples. This represents the first successful isolation and concurrent analysis of distinct intermediate species directly from a zeolite-forming gel, enabling a direct comparison of their structural evolution.

Table 1 Yield (%) of the MTW-*t*-C, MTW-*t*-HOP, MTW-*t*-POP and monomer/oligomer samples in the gel system

Time/h	24	28	32	36	40	44	48	72
MTW-*t*-C	3.2	10.4	17.5	33.8	47.6	75.7	81.2	86.2
MTW-*t*-HOP	14.7	14.1	22.2	10.4	6.4	0.5	Trace	—
MTW-*t*-POP	40.4	28.5	19.6	20.5	7.32	0	0.7	0
Monomers/oligomers	9.3	10.0	9.40	9.50	12.0	12.3	5.0	1.9
H_2O + SDA	32.3	37.1	31.3	25.7	26.7	15.0	13.0	13.0

The MTW-*t*-C series represents the early crystalline fraction of the gel. All MTW-*t*-C samples exhibit XRD patterns (Fig. 2b) consistent with those of the pure MTW phase, with significantly enhanced crystallinity compared to the parent gels (Fig. S1). This is corroborated by FT-IR spectra (Fig. 2c), where the characteristic vibration of the 12-membered ring channel system at 576 cm^{-1} is present in all samples, while the band at 950 cm^{-1} associated with structural defects[31–33] diminishes with prolonged crystallization, underscoring the framework development.

Electron microscopy (Fig. 2a) reveals that all MTW-*t*-C are mesocrystals assembled from nanocrystalline domains, unequivocally supporting a nonclassical crystallization pathway *via* particle attachment. The assembly process evolves from a loose, open structure in MTW-24-C (~520 nm) with visible, unattached nanocrystals at its periphery (Fig. 2a-1), to progressively denser and larger particles, culminating in MTW-40 (~884 nm, Fig. 2a-3).

This structural evolution is quantitatively captured by Ar physisorption (Fig. 2d and e). The type I/IV hybrid isotherms confirm micro-mesoporous architectures.[34,35] Interestingly, the texture properties do not change monotonically with the crystallization time (Table S1). This may be related to the crystallization details, which will be analyzed in depth later. MTW-24-C shows the highest uptake at high relative pressure, indicating its loose texture. The subsequent contraction in mesopore size distribution and the eventual development of a dense microstructure in MTW-72 reflect the continuous densification and structural consolidation during crystallization. Thus, the gel deconstruction-dialysis method provides direct access to crystalline zeolite intermediates with tunable particle size, porosity, and density from a single synthesis system.

In parallel, the MTW-*t*-HOP species represents a novel, short-range ordered precursor previously unidentified within worm-like precursors of the gel due to the lack of appropriate separation methods. These particles, with consistent sizes of ~10 nm (Fig. 3a), are effectively separated from large-sized MTW-*t*-C by simple centrifugation. Their structural nature is defined by a combination of techniques. XRD patterns (Fig. 3b) display broad peaks in regions corresponding to MTW zeolite

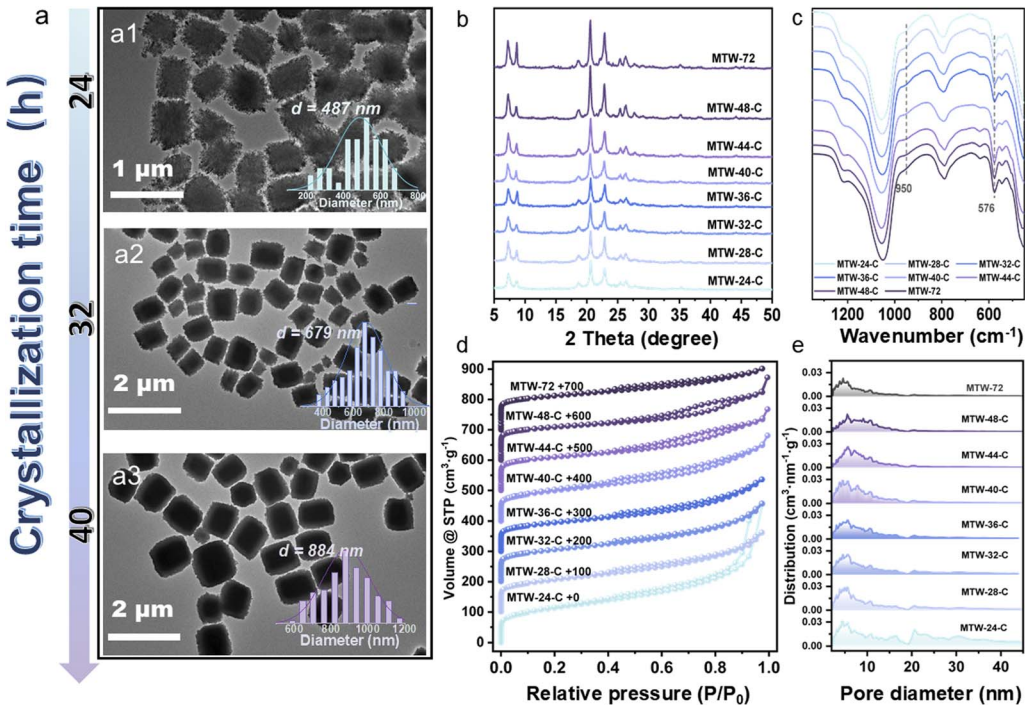

Fig. 2 Characterization of the MTW-*t*-C species. The (a) high resolution TEM images, inset: the size distributions of MTW-*t*-C. The (b) XRD and (c) FTIR spectrograms of MTW-*t*-C. The (d) Ar absorption isotherm curves of MTW-*t*-C, and the (e) pore size distribution in the mesopore range.

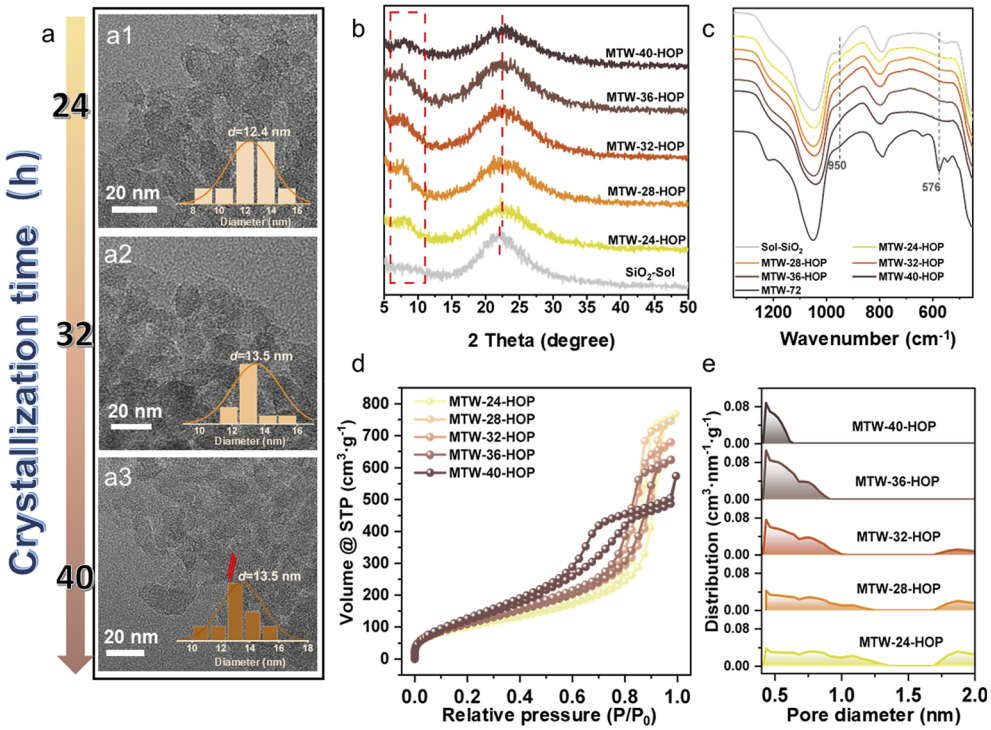

Fig. 3 Characterization of the MTW-*t*-HOP species. The (a) high resolution TEM images, inset: the size distributions of MTW-*t*-HOP. The (b) XRD and (c) FTIR spectrograms of MTW-*t*-HOP. The (d) Ar absorption isotherm curves of MTW-*t*-HOP, and the (e) pore size distribution in the micropore range.

reflections, distinct from the featureless SiO_2 sol, indicating the emergence of short-range order. As FT-IR spectra (Fig. 3c) confirmed, the absence of the 576 cm^{-1} band precludes a fully formed 12-MR channel, but the significantly weakened 950 cm^{-1} band relative to structure defects signifies a structured, non-amorphous state. Direct evidence comes from TEM images (Fig. S10c and d), where lattice fringes become apparent in later-stage MTW-*t*-HOP samples (t = 40–48), albeit limited to small (20–30 nm) or distorted over large (about 40–50 nm) domains. Critically, Ar physisorption (Fig. 3d and e and Table S2) unambiguously demonstrates the development of primary micropores within these nanoparticles. The narrowing micropore size distribution, which progressively converges towards that of the mature MTW zeolite, reflects the continuous enhancement of short-range order during crystallization—a trend also mirrored in the evolving mesopore structure (Fig. S11). The existence of this defined, yet non-crystalline, microporous structure explains the retention of HOP species during dialysis and infers them as the crucial building blocks in the nonclassical assembly process. The existence of this type of short-range ordered precursor species is consistent with the phenomena predicted in recent molecular simulations.[30,36] These unique short-range ordered precursors, possessing incipient zeolitic micropores and high external surface areas, present promising opportunities as novel catalytic carriers.

The acidic properties of the isolated intermediates, crucial for catalysis, were probed by NH_3-TPD and Py-IR. The MTW-*t*-C series exhibited a progressive development of acidity alongside crystallinity (Fig. S12a and b). Both the population and strength of weak and strong acid sites increased with crystallization time. In addition, all MTW-*t*-C samples contained both Brønsted (B) and Lewis (L) acid sites, with the B/L ratio increasing systematically as the framework matured, reflecting the formation of a more defined and fully connected aluminosilicate network.

Disentangling and simulating the interwoven crystallization in gels

The quantitative tracking of all isolated species (MTW-*t*-C, HOPs, POPs, and monomers/oligomers; Table 1) and MTW-*t*-C size (Fig. S13) allows for a more comprehensive reconstruction of the crystallization pathway (Fig. 4a) than does the crystallization kinetic curve. Analysis of the relative crystallinity and species dynamics reveals three distinct stages: (i) prolonged induction and nucleation (before 24 h), (ii) particle attachment (24–40 h), and (iii) molecular addition (after 40 h). Throughout the whole induction period, the entire system retains an extremely low degree of relative crystallinity. It is only after entering the attachment period that the crystallinity and the yield of MTW-*t*-C increase rapidly. This may be due to the rapid formation of crystal nuclei at locally supersaturated sites within the gel[37,38] in the end of the induction period. Given the challenge of probing the uncontrollable nucleation stage, we focus our mechanistic analysis on the subsequent growth periods. The temporal evolution of the species yields provides direct evidence for the interweaving of non-classical (particle

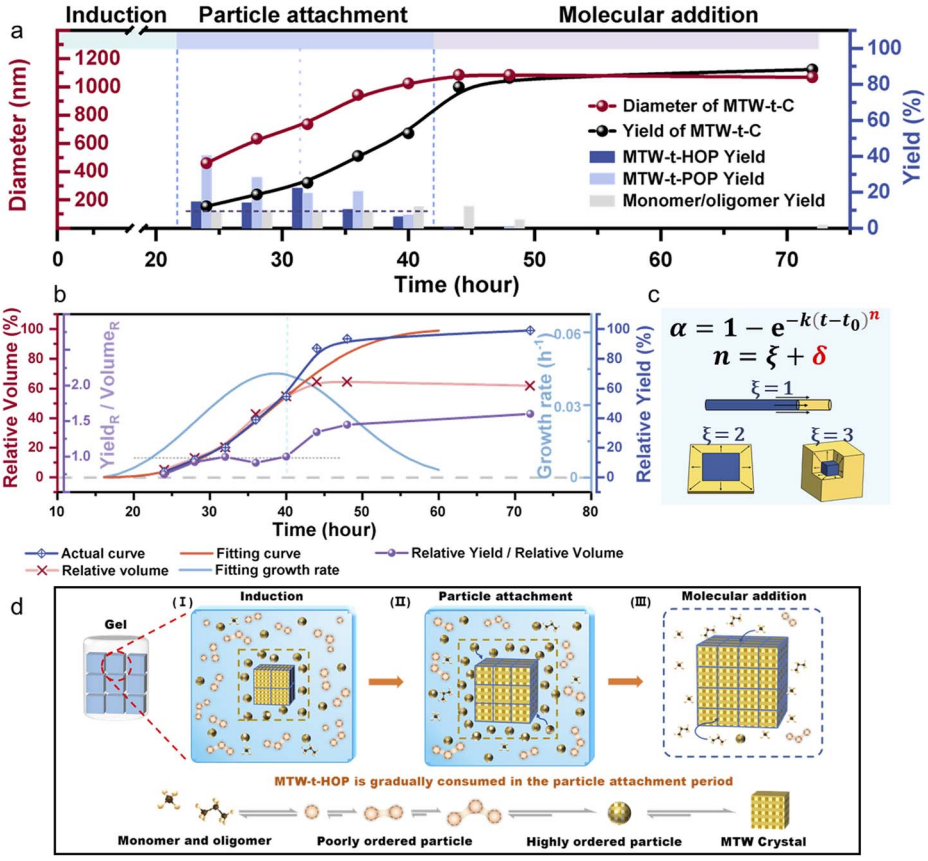

Fig. 4 Disentangling and simulating the interwoven crystallization. (a) The yield (black curve) and size (red curve) of MTW-*t*-C samples, and the yield of the other species involved with different hydrothermal times in the gel. (b) The actual curve of the MTW-*t*-C zeolite samples' relative yield (blue line) or relative volume (red line), and the curve of the ratio of the relative yield to the relative volume (purple line); the fitting curve of relative yield (orange line) and corresponding fitting growth rate (light blue line) when the relative yield of MTW-*t*-C simulated by the KJMA model is 24–40 hours of hydrothermal treatment. (c) The growth patterns of different ξ values. (d) Schematic diagram of MTW zeolite growth in the gel.

attachment) and classical (molecular addition) mechanisms. During the particle attachment stage (24–40 h), the constant level of monomers/oligomers (Fig. 4a, grey bar) implies their negligible involvement. Instead, the synchronous increase in MTW-*t*-C yield (black line) and particle size (red line) is driven by the attachment of particulate species. Additionally, the particle size of MTW-*t*-C increases linearly during the particle attachment period (red curve in Fig. 4a), which means that the dynamic behaviour of attachment species is consistent, and they are uniformly attached to the zeolite surface layer by layer in each dimension, resulting in rapid crystal growth. The MTW-*t*-HOP yield (blue bar) initially increases (24–32 h) as its formation from POPs (light blue bar, whose yield is constantly decreasing) surpasses its consumption to C and then decreases (32–44 h) as consumption outstrips supply. This inverse correlation highlights POPs as the nutrient reservoir for HOPs, while HOPs in turn serve as the direct building blocks for crystal growth. The molecular addition stage (after 40 h) is triggered by gel collapse. This is marked by a surge and subsequent consumption of monomers/oligomers, alongside a continued rise in MTW-*t*-C yield (black line) despite the depletion of HOPs and stabilization of crystal size. The mass balance confirms that the crystallinity increase in this stage is primarily due to molecular addition.

To quantitatively analyze the kinetics of the particle attachment stage, we applied the Kolmogorov–Johnson–Mehl–Avrami (KJMA) model.[39–42] The relative yield of MTW-*t*-C during the 24–40 h interval was used as the transformed fraction, α, for fitting (Fig. 4b). The excellent agreement between the model (orange curve) and experimental data ($R^2 = 0.994$, Fig. S14) validates the application of the KJMA model to this stage. The significant deviation after 40 hours provides quantitative confirmation of the mechanistic shift to molecular addition. The Avrami exponent, n, offers insight into the crystallization mode (Fig. 4c). Given the three-dimensional growth of MTW crystals ($\zeta = 3$), the fitted parameter indicates instantaneous nucleation ($\delta = 0$), meaning that all nuclei were generated before 24 h. This is highly consistent with the "barrierless nucleation" mechanism proposed in recent classical nucleation theory calculations and coarse-grained molecular simulations, which suggest that the nucleation barrier for zeolite formation from amorphous precursors is extremely small, allowing instantaneous nucleation.[30,36] The yield growth rate (light blue curve, Fig. 4b) peaks at the point where HOP species become depleted and the gel collapses. This correlation confirms that HOPs are the key

attached species governing the growth rate, as the demand for HOPs increases with the cube of the crystal size during 3D growth, eventually outpacing supply, which caused a transformation in the crystallization mechanism.

Further supporting the instantaneous nucleation mechanism derived from the KJMA model, we analyzed the correlation between the relative yield and relative volume of MTW-*t*-C samples (Formula S1). Assuming constant particle density in the particle attachment stage, a yield-to-volume ratio of 1 implies a constant number of growing crystals. As depicted in Fig. 4b, the relative yield of MTW-*t*-C (blue curve) and its relative volume (red curve) have a synchronous increase, and their ratio (purple curve) is close to 1 throughout the particle attachment process. The notable deviation for MTW-24-C is consistent with its initially loose and poorly densified structure, as previously observed. Once this initial stage passes, the stable ratio confirms that no new nuclei form after 24 hours, and the entire growth process proceeds solely *via* the attachment of species, primarily MTW-*t*-HOP, to these pre-existing nuclei. However, after 40 hours, the molecular addition stage started. As the particle size of MTW-*t*-C species remained unchanged, the monomer/oligomer species were continuously added to the zeolite framework leading to an increase in the density of MTW-*t*-C, resulting in a continuous increase in the ratio of relative yield to relative volume. This decoupling of nucleation and growth stages validates the MTW gel system as a robust model for disentangling crystallization mechanisms in complex gels.

To sum up, by deconstructing the gel and quantitatively tracking all species, we have delineated the crystallization of MTW zeolite into three consecutive stages: nucleation, particle attachment, and molecular addition, as schematically summarized in Fig. 4d.

1. The gel initially forms a solid-like network that confines the mobility of aluminosilicate species. Our data, including the KJMA model analysis and the constant yield-to-volume ratio of MTW-*t*-C, confirm that instantaneous nucleation occurs before 24 h, generating all crystal nuclei upfront (Fig. 4d-I).

2. The subsequent particle attachment stage (24–40 h) is dominated by a nonclassical mechanism. Within the confined gel network, crystal growth proceeds primarily through the direct attachment of short-range-ordered MTW-*t*-HOP particles—identified as the key building blocks—to the existing nuclei (Fig. 4d-II). The consumption of HOPs is balanced by their continuous replenishment from the reservoir of poorly ordered POP species, maintaining a dynamic equilibrium.[43,44]

3. Ultimately, the large-scale conversion of precursors into zeolites triggers gel disintegration at about 40 h, marking the onset of the molecular addition stage. The collapse of the network liberates confined species and water molecules, transitioning the system to a solution-dominated environment (Fig. 4d-III). This removes the spatial restrictions for MTW-*t*-HOP attachment and facilitates a classical crystallization pathway *via* monomers/oligomers.[11] This mechanistic shift explains the most significant boost in MTW-*t*-C yield during 40–44 h, even as the HOP population is nearly depleted.

Competing dynamics of particle attachment/structural maturation

While the attachment of MTW-*t*-HOP precursors directly drives the rapid increase in MTW-*t*-C size, the non-monotonic evolution of texture properties (*e.g.*, porosity and defects) points to a more complex dynamic. We find that the final zeolite properties emerge from a continuous competition between the kinetics of HOP attachment and the thermodynamics of structural rearrangement and dealumination.

The dynamic competition between attachment and maturation is quantitatively captured by the evolving elemental composition. The higher and fluctuating bulk Si/Al ratio of MTW-*t*-C (38–55) reveals that significant dealumination must occur after attachment to achieve the composition of the mature MTW framework. However, at the same moment, the surface Si/Al ratio of MTW-*t*-C is always lower than the bulk phase Si/Al ratio, indicating that the surface is relatively more aluminium-rich (Fig. 5a). This is because MTW-*t*-HOP species with a lower Si/Al ratio (16–21) are attached to the surface as direct building blocks and then start to improve the structure through the dealumination process, but the degree of dealumination is not as good as that inside the sample. This inside-out Al gradient (also reflected in TEM element analysis in Fig. S15 and Table S3) and the non-monotonic trend in bulk Si/Al are direct signatures of the competing rates. During the early particle attachment stage, slow attachment permits efficient dealumination, raising the Si/Al ratio, whereas later rapid attachment leads to the accumulation of Al-rich HOPs, lowering the apparent ratio. Upon the transition to the molecular addition stage, the solution-phase environment enables efficient dealumination, driving the Si/Al ratio upward as the crystal approaches its thermodynamic equilibrium.

UV-Raman and solid-state NMR spectroscopy provide molecular-level validation of this mechanism. The high relative abundance of 4-membered rings (4 MR at 460 cm^{-1})[45] in both early MTW-*t*-C and MTW-*t*-HOP (Fig. 5b and c) confirms the direct incorporation of HOP building blocks. The subsequent surface enrichment[46–48] of relatively silicon-rich 5 MR and 6 MR at 403 cm^{-1} and 362 cm^{-1} respectively[45] in later-stage MTW-*t*-C signals the solution-phase-mediated reconstruction of the framework into the correct MTW topology. Concurrently, ^{29}Si MAS NMR (Fig. 5d and e) traces the elimination of silanol defects, shown by a steadily increasing Q^4/Q^3 ratio (−104 ppm for Si–OH defected Q^3 (0Al) and −111 ppm for Q^4 (0Al) species).[49,50] The stagnation at 1.5 of the Q^4/Q^3 ratio in MTW-*t*-C during the period of rapid HOP attachment (28–40 h) reflects the dominance of multi-defect HOPs' kinetic incorporation. The marked increase in this ratio upon gel disintegration underscores the superior defect-healing capability of the solution-phase molecular addition process. It is precisely this molecular-level structural rearrangement ability that determines the final degree of defect healing and framework improvement.[51]

This kinetic-thermodynamic competition is also vividly captured by TEM (Fig. 6a and S16). In the early particle attachment stage (24–32 h), the intermediate product of MTW-

24-C exhibits irregular morphologies and misoriented lattice domains, indicative of non-oriented HOP attachment (Fig. 6a-1). As growth proceeds, the slow attachment rate allows for sufficient structural reorganization, leading to improved crystallinity and penetrating lattice fringes in MTW-32-C (Fig. 6a-2). However, between 32 and 40 h, a surge in the HOP attachment rate (evidenced by the rapid yield increase) outpaces the restructuring capacity, re-introducing lattice disorder in MTW-40-C (Fig. 6a-3).

This imbalance is rectified upon gel collapse and the onset of molecular addition (40–72 h). The solution-phase environment facilitates rapid interfacial recrystallization, yielding MTW-44-C/MTW-72 particles with uniform lattice fringes and sharp, well-defined facets (Fig. 6a-4 and a-5), underscoring the critical role of the solution phase in defect healing.

The pore structure evolution provides quantitative corroboration of this mechanism and can be explained now. The micropore volume of MTW-*t*-C (Fig. 2d, Table S1) mirrors the structural competition: it increases during the slow-attachment/rearrangement-dominant phase (24–32 h), decreases when rapid attachment introduces defects (32–40 h), and surges most significantly after gel collapse due to the defect-healing action of molecular addition. Further evidence comes from the dynamic changes in the micropore size distribution (Fig. S17). The distribution first sharpens (24–32 h) as maturation creates a uniform pore network, then broadens (32–40 h) due to disordered stacking from fast attachment, and finally intensifies without broadening post-40 h as molecular infusion repairs the framework. Besides, mesopore volume follows a complementary trajectory (Fig. 2e), initially decreasing from densification, then increasing from disordered stacking, and finally decreasing again as solution-phase processes promote consolidation.

In conclusion, the crystallization of MTW zeolite in gels is governed by the dynamic competition between the kinetics of HOP attachment and the thermodynamics of structural maturation and dealumination (Fig. 6b). This framework rationalizes the roles of all species: long-range-ordered crystals (C) as an interface for species attachment, poorly ordered particles (POPs) as a nutrient pool, short-range but highly ordered precursors (HOPs) as the primary building blocks for non-classical growth, and monomers/oligomers as the agents for classical crystal perfection. The gel collapse is identified as the critical event that shifts the system from an attachment-limited, solid-like regime to a rearrangement-facilitated, solution-dominated regime. This mechanistic understanding, enabled

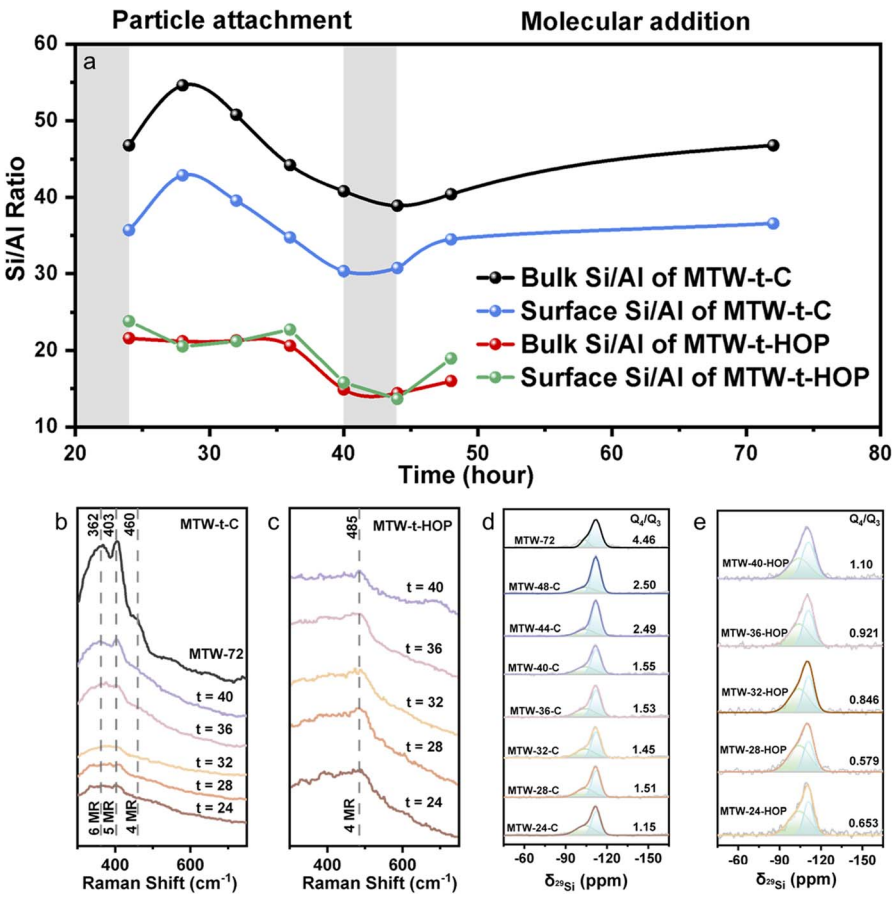

Fig. 5 Detailed characterization of the MTW-*t*-C intermediate species. (a) The bulk Si/Al ratio (black line) or surface Si/Al ratio (blue line) of MTW-*t*-C zeolites and bulk (red line) or surface (green line) Si/Al ratio of MTW-*t*-HOP in the gel. The UV-Raman spectra of (b) MTW-*t*-C and (c) MTW-*t*-HOP at different hydrothermal times. The ^{29}Si MAS NMR spectra of (d) MTW-*t*-C and (e) MTW-*t*-HOP at different hydrothermal times.

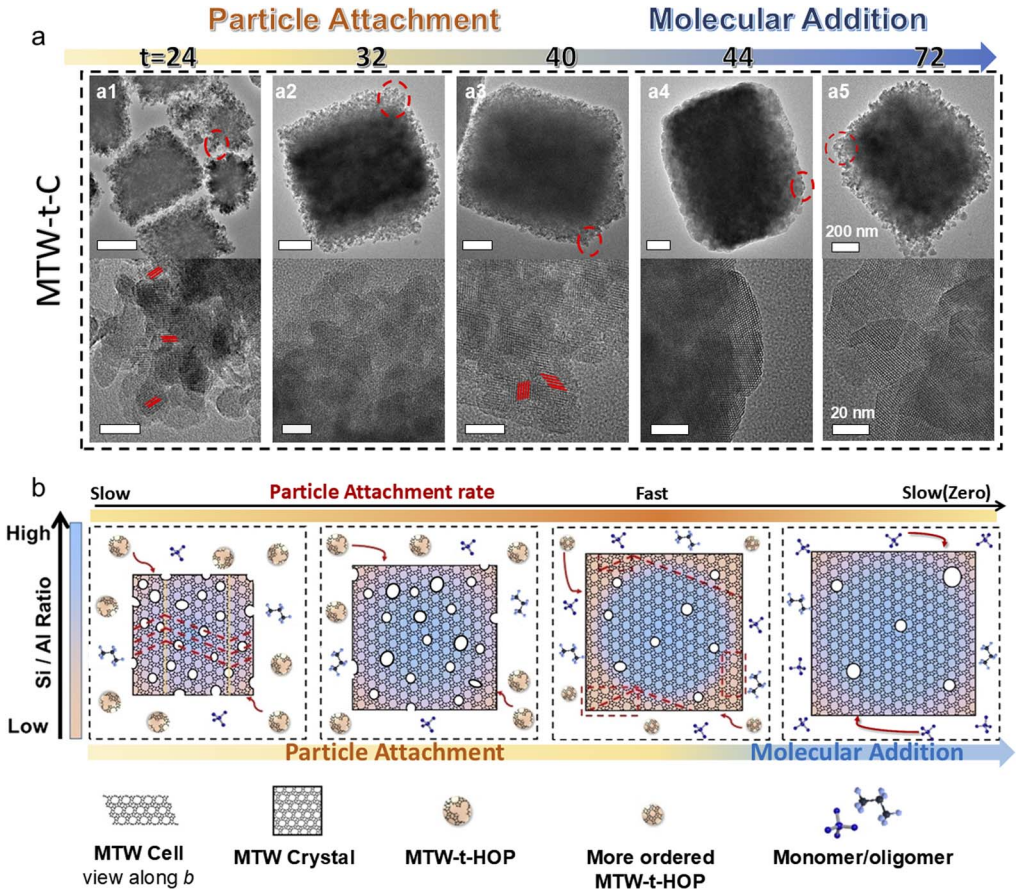

Fig. 6 The competition between dynamics and thermodynamics within the system. (a) TEM images of MTW-*t*-C samples at different hydrothermal times. The detailed images of the red circles in the upper series are shown in the nether series. (b) The effect of MTW-*t*-HOP's attachment behavior on the structure, element composition and status of MTW-*t*-C zeolite in the gel.

by our gel deconstruction approach, deciphers the complex interplay of species and processes within the zeolite synthesis "black box" in gel-based systems.

Conclusions

In this work, we have unlocked the "black box" of gel-based zeolite crystallization by developing a generalizable deconstruction-dialysis method. This approach enables the quantitative isolation and characterization of all particulate species—crystals (C), highly ordered precursors (HOPs), poorly ordered particles (POPs), and soluble monomers/oligomers—from a complex gel network.

This comprehensive speciation allows us to propose a refined crystallization mechanism with three distinct stages: (i) initial instantaneous nucleation, (ii) a nonclassical growth stage dominated by the attachment of HOP particles to the crystals, and (iii) a final molecular addition stage initiated by gel collapse. Crucially, we identify HOPs as the key nutrient for growth and POPs as their reservoir.

Beyond mapping the pathway, we uncover the central role of kinetic-thermodynamic competition. The properties of the final product (morphology, porosity and composition) are not predetermined but emerge from the dynamic competition between the kinetics of HOP attachment and the thermodynamics of structural rearrangement and dealumination. The gel network modulates this competition by confining species mobility, while its collapse releases this constraint, shifting the dominant mechanism.

This study transforms the gel from an opaque medium into a legible system where speciation and dynamics are quantifiable. The insights and methodologies presented herein provide a foundational framework for the precursor-directed, rational design of zeolites, bridging a long-standing gap between industrial synthesis practices and fundamental materials science. And it also exhibits potential generalizability in other zeolite gels with different Si/Al ratios (Fig. S18 and S19) and different topologies (Fig. S20).

Author contributions

Kexin Yan and Feng Lin: conceptualization, investigation, data curation, formal analysis, writing – original draft, visualization. Zhaoqi Ye and Yifan Zhang: formal analysis, data curation. Yang Zhao, Zhangping Shi, Di Pan: investigation, methodology, validation. Yahong Zhang: resources, formal analysis, writing –

review and editing. Hongbin Zhang: resources, conceptualization, formal analysis, visualization, writing – review and editing. Yi Tang: resources, formal analysis, writing – review and editing, supervision, project administration.

Conflicts of interest

There are no conflicts to declare

Data availability

The data supporting this article have been included as part of the supplementary information (SI). Supplementary information: synthesis, characterization instrument information, the XRD patterns and TEM and SEM images of the MTW-*t*-Gel, C and HOP samples, the texture information and pore size distribution of the MTW-*t*-C and HOP samples, the particle size distribution of the MTW-*t*-C and HOP samples and the logarithmically fitted Avrami equation. See DOI: https://doi.org/10.1039/d6sc02206e.

Acknowledgements

This work was supported by the National Key R&D Program of China (no. 2023YFA1507602 to Yi Tang), the National Natural Science Foundation of China (nos. 22088101 to Yi Tang, 22175040 to HongBin Zhang, and 22402036 to Zhaoqi Ye), and the Science and Technology Commission of Shanghai Municipality (no. 2024ZDSYS02 to Yi Tang).

Notes and references

1 J. Čejka, G. Centi, J. Perez-Pariente and W. J. Roth, Zeolite-based materials for novel catalytic applications: Opportunities, perspectives and open problems, *Catal. Today*, 2012, **179**, 2.

2 J. Shi, Y. Wang, W. Yang, Y. Tang and Z. Xie, Recent advances of pore system construction in zeolite-catalyzed chemical industry processes, *Chem. Soc. Rev.*, 2015, **44**, 8877.

3 L. I. Rodionova, E. E. Knyazeva, S. V. Konnov and I. I. Ivanova, Application of Nanosized Zeolites in Petroleum Chemistry: Synthesis and Catalytic Properties (Review), *Pet. Chem.*, 2019, **59**, 455.

4 D. Stosic and V. Zholobenko, Application of Zeolite-Based Materials for Chemical Sensing of VOCs, *Sensors*, 2025, **25**, 1634.

5 Y. Yao, H. Cheng, G. Zhong, X. Tang, H. Yi, S. Zhao, F. Gao and Q. Yu, Progress in the construction strategy of noble metal active sites for zeolite-based PNA and VOCs catalysts, *Green Energy Environ.*, 2025, **10**, 709.

6 N. Yuan, L. Han, X. Zhang, H. Liang and Y. Liu, Synergistic preparation of zeolite A from coal gasification coarse slag and red mud for the adsorptive removal of organic dyes, *J. Ind. Eng. Chem.*, 2025, **149**, 692.

7 P. A. Jacobs, M. Dusselier and B. F. Sels, Will zeolite-based catalysis be as relevant in future biorefineries as in crude oil refineries?, *Angew Chem. Int. Ed. Engl.*, 2014, **53**, 8621.

8 L. Ren, Q. Wu, C. Yang, L. Zhu, C. Li, P. Zhang, H. Zhang, X. Meng and F. S. Xiao, Solvent-free synthesis of zeolites from solid raw materials, *J. Am. Chem. Soc.*, 2012, **134**, 15173.

9 T. M. Davis, T. O. Drews, H. Ramanan, C. He, J. Dong, H. Schnablegger, M. A. Katsoulakis, E. Kokkoli, A. V. McCormick, R. L. Penn and M. Tsapatsis, Mechanistic principles of nanoparticle evolution to zeolite crystals, *Nat. Mater.*, 2006, **5**, 400.

10 A. I. Lupulescu and J. D. Rimer, In Situ Imaging of Silicalite-1 Surface Growth Reveals the Mechanism of Crystallization, *Science*, 2014, **344**, 729.

11 Z. Sheng, H. Li, K. Du, L. Gao, J. Ju, Y. Zhang and Y. Tang, Observing a Zeolite Nucleus (Subcrystal) with a Uniform Framework Structure and Its Oriented Attachment without Single-Molecule Addition, *Angew Chem. Int. Ed. Engl.*, 2021, **60**, 13444.

12 K. Du, X. Zhang, T. He, W. Shen, H. Xu, Y. Tang, X. M. Cao, Z. Huang and Y. Zhang, Dynamic Evolution of Structural Ordering and Aluminum Redistribution During ZSM-5 Zeolite Crystallization, *Angew Chem. Int. Ed. Engl.*, 2025, **64**, e202507223.

13 Q. Zhang, A. Mayoral, O. Terasaki, Q. Zhang, B. Ma, C. Zhao, G. Yang and J. Yu, Amino Acid-Assisted Construction of Single-Crystalline Hierarchical Nanozeolites via Oriented-Aggregation and Intraparticle Ripening, *J. Am. Chem. Soc.*, 2019, **141**, 3772.

14 M. Alonso-Doncel, A. Peral, C. Ochoa-Hernandez, R. Sanz and D. P. Serrano, Tracking the evolution of embryonic zeolites into hierarchical ZSM-5, *J. Mater. Chem. A*, 2021, **9**, 13570–13587.

15 K.-G. Haw, J.-P. Gilson, N. Nesterenko, M. Akouche, H. El Siblani, J.-M. Goupil, B. Rigaud, D. Minoux, J.-P. Dath and V. Valtchev, Supported Embryonic Zeolites and Their Use to Process Bulky Molecules, *ACS Catal.*, 2018, **8**, 8199.

16 M. Akouche, J.-P. Gilson, N. Nesterenko, S. Moldovan, D. Chateigner, H. El Siblani, D. Minoux, J.-P. Dath and V. Valtchev, Synthesis of Embryonic Zeolites with Controlled Physicochemical Properties, *Chem. Mater.*, 2020, **32**, 2123.

17 H. Li, J. Yu, K. Du, W. Li, L. Ding, W. Chen, S. Xie, Y. Zhang and Y. Tang, Synthesis of ZSM-5 Zeolite Nanosheets with Tunable Silanol Nest Contents across an Ultra-wide pH Range and Their Catalytic Validation, *Angew Chem. Int. Ed. Engl.*, 2024, **63**, e202405092.

18 J. Yu, K. Du, D. Pan, H. Li, L. Ding, W. Chen, Y. Zhang and Y. Tang, Distinguishing and unraveling classical and non-classical pathways in MFI zeolite crystallization: insights into their contributions and impact on the final product, *Inorg. Chem. Front.*, 2025, **12**, 4048.

19 J. J. De Yoreo, P. U. Gilbert, N. A. Sommerdijk, R. L. Penn, S. Whitelam, D. Joester, H. Zhang, J. D. Rimer, A. Navrotsky, J. F. Banfield, A. F. Wallace, F. M. Michel, F. C. Meldrum, H. Colfen and P. M. Dove, CRYSTAL GROWTH. Crystallization by particle attachment in synthetic, biogenic, and geologic environments, *Science*, 2015, **349**, aaa6760.

20 N. Ren, S. Bosnar, J. Bronic, M. Dutour Sikiric, T. Misic, V. Svetlicic, J. J. Mao, T. Antonic Jelic, M. Hadzija and B. Subotic, Role of subcolloidal (nanosized) precursor species in the early stage of the crystallization of zeolites in heterogeneous systems, *Langmuir*, 2014, **30**, 8570.

21 N. Ren, B. Subotić, J. Bronić, Y. Tang, M. Dutour Sikirić, T. Mišić, V. Svetličić, S. Bosnar and T. Antonić Jelić, Unusual Pathway of Crystallization of Zeolite ZSM-5 in a Heterogeneous System: Phenomenology and Starting Considerations, *Chem. Mater.*, 2012, **24**, 1726.

22 Y. Li, Y. Zhang, A. Lan, H. Bian, R. Liu, X. Li, P. Han and T. Dou, Synthesis of SSZ-13 zeolite with zeolite L-added synthesis gel absent from additional aluminum source, *Microporous Mesoporous Mater.*, 2019, **279**, 1.

23 Z. Ye, L. Kong, Y. Zhao, C. Zhang, X. Yang, K. Yan, Y. Zhang, H. Zhang and Y. Tang, Alkalinity-controlled zeolite nucleation and growth: ultrafast synthesis of total-morphology zeolite L mesocrystals and adsorption evaluation, *Chem. Synth.*, 2022, **2**, 20.

24 Y. Zhao, H. Zhang, P. Wang, F. Xue, Z. Ye, Y. Zhang and Y. Tang, Tailoring the Morphology of MTW Zeolite Mesocrystals: Intertwined Classical/Nonclassical Crystallization, *Chem. Mater.*, 2017, **29**, 3387.

25 K. Yan, Y. Zhao, C. Zhao, H. Li, Z. Ye, X. Yang, Y. Zhang, H. Zhang and Y. Tang, K^+ promoted fabrication of nanoneedle low-silicon ZSM-48 mesocrystal, *Chem. Synth.*, 2024, **4**, 38.

26 R. Jain, Z. Niu, M. Choudhary, H. Bourji, J. C. Palmer and J. D. Rimer, In Situ Imaging of Faujasite Surface Growth Reveals Unique Pathways of Zeolite Crystallization, *J. Am. Chem. Soc.*, 2023, **145**, 1155.

27 M. Kumar, R. Li and J. D. Rimer, Assembly and Evolution of Amorphous Precursors in Zeolite L Crystallization, *Chem. Mater.*, 2016, **28**, 1714.

28 Z. Ye, Y. Zhao, H. Zhang, Z. Shi, H. Li, X. Yang, L. Wang, L. Kong, C. Zhang, Z. Sheng, Y. Zhang and Y. Tang, Mesocrystal morphology regulation by "alkali metals ion switch": Re-examining zeolite nonclassical crystallization in seed-induced process, *J. Colloid Interface Sci.*, 2022, **608**, 1366.

29 K. Yan, Z. Ye, L. Kong, H. Li, X. Yang, Y. Zhang, H. Zhang and Y. Tang, Seed-Induced Synthesis of Disc-Cluster Zeolite L Mesocrystals with Ultrashort c-Axis: Morphology Control, Decoupled Mechanism, and Enhanced Adsorption, *Acta Phys.-Chim. Sin.*, 2024, **40**, 2308019.

30 D. Dhabal, S. Banik, A. A. Bertolazzo, H. Chan, S. K. R. S. Sankaranarayanan and V. Molinero, Barrierless nucleation in glassy precursors drives zeolite formation, *Proc. Natl. Acad. Sci. U. S. A.*, 2025, **122**(49), e2506679122.

31 S. Jegatheeswaran, C. M. Cheng and C. H. Cheng, Effects of adding alcohols on ZSM-12 synthesis, *Microporous Mesoporous Mater.*, 2015, **201**, 24.

32 G. Feng, Z.-H. Wen, J. Wang, Z.-H. Lu, J. Zhou and R. Zhang, Guiding the design of practical MTW zeolite catalysts: An integrated experimental-theoretical perspective, *Microporous Mesoporous Mater.*, 2021, **312**, 110810.

33 T. D. Courtney, C.-C. Chang, R. J. Gorte, R. F. Lobo, W. Fan and V. Nikolakis, Effect of water treatment on Sn-BEA zeolite: Origin of 960 cm^{-1} FTIR peak, *Microporous Mesoporous Mater.*, 2015, **210**, 69.

34 H. Zhang, K. Song, L. Wang, H. Zhang, Y. Zhang and Y. Tang, Organic Structure Directing Agent-Free and Seed-Induced Synthesis of Enriched Intracrystal Mesoporous ZSM-5 Zeolite for Shape-Selective Reaction, *ChemCatChem*, 2013, **5**, 2874.

35 H. Zhang, Y. Zhao, H. Zhang, P. Wang, Z. Shi, J. Mao, Y. Zhang and Y. Tang, Tailoring Zeolite ZSM-5 Crystal Morphology/Porosity through Flexible Utilization of Silicalite-1 Seeds as Templates: Unusual Crystallization Pathways in a Heterogeneous System, *Chem.–Eur. J.*, 2016, **22**, 7141.

36 D. Dhabal, A. A. Bertolazzo and V. Molinero, Coarse-Grained Model for the Hydrothermal Synthesis of Zeolites, *J. Phys. Chem. C*, 2021, **125**, 26857–26868.

37 S. I. Zones, K. Jayanthi, J. Pascual, D. Xie and A. Navrotsky, Energetics of the Local Environment of Structure-Directing Agents Influence Zeolite Synthesis, *Chem. Mater.*, 2021, **33**, 2126.

38 S. Lee, C. T. Nimlos, E. R. Kipp, Y. Wang, X. Gao, W. F. Schneider, M. Lusardi, V. Vattipalli, S. Prasad, A. Moini and R. Gounder, Evolution of Framework Al Arrangements in CHA Zeolites during Crystallization in the Presence of Organic and Inorganic Structure-Directing Agents, *Cryst. Growth Des.*, 2022, **22**, 6275.

39 M. Tomellini and M. Fanfoni, Connection between phantom and spatial correlation in the Kolmogorov–Johnson–Mehl–Avrami-model: A brief review, *Phys. A*, 2022, **590**, 126748.

40 P. F. Corregidor, D. E. Acosta and H. A. Destéfanis, Kinetic Study of Seed-Assisted Crystallization of ZSM-5 Zeolite in an OSDA-Free System Using a Natural Aluminosilicate as Starting Source, *Ind. Eng. Chem. Res.*, 2018, **57**, 13713.

41 R. W. Thompson, Analysis of zeolite crystallizations using Avrami transformation methods, *Zeolites*, 1992, **12**, 680.

42 P. Zhang, S. Li, P. Guo and X. Zhao, Synthesis of ZSM-5 Microspheres Made of Nanocrystals from Iron Ore Tailings by the Solid-Phase Conversion Method, *Langmuir*, 2020, **36**, 6160.

43 K. N. Olafson, R. Li, B. G. Alamani and J. D. Rimer, Engineering Crystal Modifiers: Bridging Classical and Nonclassical Crystallization, *Chem. Mater.*, 2016, **28**, 8453.

44 R. Li, A. Chawla, N. Linares, J. G. Sutjianto, K. W. Chapman, J. G. Martínez and J. D. Rimer, Diverse Physical States of Amorphous Precursors in Zeolite Synthesis, *Ind. Eng. Chem. Res.*, 2018, **57**, 8460.

45 Y. Yu, G. Xiong, C. Li and F. Xiao, Characterization of aluminosilicate zeolites by UV Raman spectroscopy, *Microporous Mesoporous Mater.*, 2001, **46**, 23.

46 W. Su, Z. Feng, T. Chen, P. Ying and C. Li, Surface Phases of TiO2 Nanoparticles Studied by UV Raman Spectroscopy and FT-IR Spectroscopy, *J. Phys. Chem. C*, 2008, **112**, 7710.

47 X. Meng, Z. Bi, P. Lou and G. Shang, Tracking Electrochemical-Cycle-Induced Surface Structure

Evolutions of Cathode Material $LiMn_2O_4$ with Improved Operando Raman Spectroscopy, *Langmuir*, 2022, **38**, 3887.

48 X. Chen, M. Song, L. Zhang, R. Zhang, L. Zhang, W. Tong, Y. Han, X. Gao, Y. Xiong, H. Xu and L. Cao, Defect-Dependent Surface Phase Transformation on 1T-TiS_2 Assisted by Water, *J. Phys. Chem. C*, 2023, **127**, 3462.

49 N. Masoumifard, S. Kaliaguine and F. Kleitz, Synergy between structure direction and alkalinity toward fast crystallization, controlled morphology and high phase purity of ZSM-12 zeolite, *Microporous Mesoporous Mater.*, 2016, **227**, 258.

50 B. Gil, Ł. Mokrzycki, B. Sulikowski, Z. Olejniczak and S. Walas, Desilication of ZSM-5 and ZSM-12 zeolites: Impact on textural, acidic and catalytic properties, *Catal. Today*, 2010, **152**, 24.

51 A. A. Bertolazzo, D. Dhabal and V. Molinero, Polymorph Selection in Zeolite Synthesis Occurs after Nucleation, *J. Phys. Chem. Lett.*, 2022, **13**, 977–981.